

A Consideration on Lander's Motion Estimation from Range Image Sequence Utilizing LRF

Koki Fujita and Shinji Hokamoto

Department of Aeronautics and Astronautics, Kyushu University

744, Motoooka, Nishi-ku, Fukuoka, 819-0395, Japan

Abstract: This study proposes a new approach to lander's motion estimation, utilizing 'range image' sequence acquired from 2D scanning Laser Range Finder (LRF) during the descent phase. Since range image can be considered as pixel data of CCD camera which contains range information instead of its original luminance one, Computer Vision theories can be applied to estimate 6 Degree-Of-Freedom (6DOF) motion of lander on which LRF is mounted. Focusing on a simulation study, 2D scanning LRF which can obtain range images with enough high resolution and high scanning rate is dealt in this paper. The effectiveness of the proposed method is demonstrated through a series of numerical simulations utilizing synthetic terrain data and range images, and some present issues are discussed.

LRFによる距離画像データを用いた着陸機運動パラメータ推定法の検討

藤田 浩輝, 外本 伸治

九州大学 大学院工学研究院 航空宇宙工学部門

概要：2次元スキャン型のレーザーレンジファインダ (LRF) から得られる距離分布データは、「距離画像」とも呼ばれ、CCDカメラの画像輝度値を距離データに置き換えたものとみなすことができる。本研究では、コンピュータビジョンの理論に基づき、降下フェーズ中の時系列距離画像データを用いた着陸機の6自由度運動パラメータ推定法を提案する。ここでは、特に一般的なカメラ画像データを距離画像に置き換えた場合の特徴を見るために、理想的な画像解像度とスキャンレートの仕様を持つLRFを仮定し、人工的に生成した地形データを用いて、数値シミュレーションによりその有用性の確認と、現時点での問題点の検討を行う。

1 Introduction

In recent years, various methods utilizing image processing techniques have been proposed for planetary exploring spacecrafts. For example, HAYABUSA tried to carry out autonomous navigation and guidance during proximity phase with optical cameras and laser altimeter (LIDAR), and demonstrated some of its autonomous functions[1] [2].

As for spacecrafts such as lander, one of the important issues with applying camera image based guidance and navigation is errors caused by the depth information for scene in images which cannot be precisely estimated only by cameras.

Laser Range Finder (LRF) is one solution to improve such errors. In previous work, to measure accurate shapes of archaeological buildings with 2D scanning LRF mounted balloon, a method utilizing CCD camera combined with the LRF is proposed[3]. Whereas the method can estimate motion of the sensor (the balloon) as well as the targets' shapes, the computational load can be serious because of the nonlinear optimization

method for a function of a large number of variables.

Instead of using conventional imaging devices such as CCD camera, this study proposes an approach to estimating the lander's motion by range image sequence acquired from 2D scanning LRF aiming at autonomous guidance and navigation during final descent phase. Since the range image can be considered as the pixel data of CCD camera which contains range information instead of its original luminance one, Computer Vision theories can be applied. The proposed method estimates lander's 6 Degree-Of-Freedom (6DOF) motion by Extended Kalman Filter algorithm through some image processing techniques applied to the range images.

Focusing on the simulation study, this paper treats 2D scanning LRF which has desirable specifications, that is, as high resolution and high scanning rate as common CCD camera has. Finally, the effectiveness of the proposed method is demonstrated through a series of numerical simulations and some present issues are discussed.

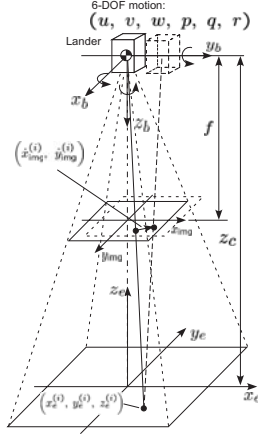


Fig. 1: Relationship between a scene point's motion in images and lander's motion.

2 Relationship between Scene Point's Motion in Range Images and Lander's Motion

In this study, to describe scene points' locations or their motion in range images, perspective projection model as shown in Fig. 1 is introduced. When a scene point at $(x_{\text{img}}, y_{\text{img}})$ in image coordinates moves at a velocity of $(\dot{x}_{\text{img}}, \dot{y}_{\text{img}})$ between two sequential images, the relationship between the scene point's velocity (well known as an 'optical flow' in Computer Vision theory), and the motion of the lander (or lander mounted LRF) can be described as follows:

$$\dot{x}_{\text{img}} = f \left\{ \left(-\frac{u}{z_c} - q + r \cdot y_{\text{img}} \right) + x_{\text{img}} \left(\frac{w}{z_c} + p \cdot y_{\text{img}} - q \cdot x_{\text{img}} \right) \right\} \quad (1)$$

$$\dot{y}_{\text{img}} = f \left\{ \left(-\frac{v}{z_c} + p - r \cdot x_{\text{img}} \right) + y_{\text{img}} \left(\frac{w}{z_c} + p \cdot y_{\text{img}} - q \cdot x_{\text{img}} \right) \right\} \quad (2)$$

where (u, v, w, p, q, r) mean the lander's velocities in 6DOF motion, and z_c denotes the scene point's position in z -axis of the body-fixed coordinates. f shows focal length of an equivalent camera, which can be calculated from field of view and resolution of the 2D scanning LRF. To simplify the model, the LRF's observing point is assumed to be coincident with gravitational center of the lander as shown in Fig. 1.

The above differential equations are called 'Image Jacobian'[4], and if external and internal parameters of imaging device, z_c and f are previously given and

optical flows for a series of the scene points in the image sequence can be obtained, the 6DOF motion of the lander can be estimated by methods such as a least squares method, Kalman Filter, etc.

However, in a case of using CCD camera, to derive the depth information (z_c) only by camera images is usually a hard task, and uncertainty remains even if some effective techniques such as Stereo Vision are applied.

On the other hand, range image acquired from LRF obviously includes the depths data for the scene points, and if they can be obtained with enough high resolution and high scanning rate, conventional image processing technique can be directly applied.

3 Lander's Motion Parameters Estimation from Range Images

Considering an optical flow of i -th scene point ($i = 1, 2, \dots$) in k -th frame ($k = 1, 2, \dots$) of range image, and z_c and w are directly measured from LRF, Eqs. (1) and (2) can be reduced into the following equations in a matrix form:

$$\begin{bmatrix} \dot{x}_{\text{img}}^{(i)}(k) - f \frac{x_{\text{img}}^{(i)}}{z_c(k)} w(k) \\ \dot{y}_{\text{img}}^{(i)}(k) - f \frac{y_{\text{img}}^{(i)}}{z_c(k)} w(k) \\ w(k) \end{bmatrix} = \begin{bmatrix} -\frac{f}{z_c(k)} & 0 & 0 & c_{14}^{(i)} & c_{15}^{(i)} & c_{16}^{(i)} \\ 0 & -\frac{f}{z_c(k)} & 0 & c_{24}^{(i)} & c_{25}^{(i)} & c_{26}^{(i)} \\ 0 & 0 & 1 & 0 & 0 & 0 \end{bmatrix} \times (u(k), v(k), w(k), p(k), q(k), r(k))^T, \quad (3)$$

where

$$\begin{aligned} c_{14}^{(i)} &= f x_{\text{img}}^{(i)}(k) y_{\text{img}}^{(i)}(k), \\ c_{15}^{(i)} &= -f \left\{ 1 + \left(x_{\text{img}}^{(i)}(k) \right)^2 \right\}, \\ c_{16}^{(i)} &= f y_{\text{img}}^{(i)}(k), \\ c_{24}^{(i)} &= -f \left\{ 1 + \left(y_{\text{img}}^{(i)}(k) \right)^2 \right\}, \\ c_{25}^{(i)} &= -f x_{\text{img}}^{(i)}(k) y_{\text{img}}^{(i)}(k), \\ c_{26}^{(i)} &= -f x_{\text{img}}^{(i)}(k). \end{aligned}$$

In the framework of Computer Vision theory, camera's motion (u, v, w, p, q, r) is estimated from the measurement data, $(\dot{x}_{\text{img}}, \dot{y}_{\text{img}})$ in Eq. (1) and (2) for

a series of scene points. These optical flows can be obtained through a tracking method[5] in image sequence, and the remaining unknown parameters, z_c are given by something except single camera image.

However, in the case of using LRF, as depth and the variation of the depth (z_c and w) can be directly measured by the range images, LRF's motion can be more effectively estimated from the measurement data on the left-hand side of Eq. (3), which is different from the image processing methods based on camera's pixel data.

If the measured variables for all d scene points in an image are denoted as,

$$\mathbf{z}(k) = \left(z_1^{(1)}(k), z_2^{(1)}(k), \dots, z_1^{(d)}(k), z_2^{(d)}(k), w(k) \right)^T, \quad (4)$$

where $z_1^{(i)}(k) = \dot{x}_{\text{img}}^{(i)}(k) - f \frac{x_{\text{img}}^{(i)}}{z_c(k)} w(k)$, $z_2^{(i)}(k) = \dot{y}_{\text{img}}^{(i)}(k) - f \frac{y_{\text{img}}^{(i)}}{z_c(k)} w(k)$ ($i = 1, 2, \dots, d$), and the motion parameters are considered as state variables such that $\mathbf{x}(k) = (u(k), v(k), w(k), p(k), q(k), r(k))^T$, the concerned system can be expressed as state and measurement equations as follows:

$$\dot{\mathbf{x}}(k) = A'(\mathbf{x}(k)) + B\mathbf{u}(k) + \mathbf{v}(k) \quad (5)$$

$$\mathbf{z}(k) = C\mathbf{x}(k) + \mathbf{w}(k) \quad (6)$$

$$k = 1, 2, \dots$$

where $\mathbf{u} \in \mathbf{R}^{6 \times 1}$ means control input for the lander's motion, and $\mathbf{v} \in \mathbf{R}^{6 \times 1}$ and $\mathbf{w}(k) \in \mathbf{R}^{d \times 1}$ denote system and measurement noises which satisfy the following expectation conditions: $E[\mathbf{v}^T \mathbf{v}] = \mathbf{S} \in \mathbf{R}^{6 \times 6}$, $E[\mathbf{w}^T \mathbf{w}] = \mathbf{T} \in \mathbf{R}^{d \times d}$.

Also, Eq. (5) describes the lander's dynamics of motion such that

$$A' = \begin{bmatrix} -qw + rv \\ -ru + pw \\ -pv + qu \\ J_{p1}qr + J_{p2}pq \\ J_{q1}(p^2 - r^2) + J_{q2}rp \\ J_{r1}qr + J_{r2}pq \end{bmatrix}, \quad (7)$$

$$B = \begin{bmatrix} 1/m & 0 & 0 & 0 & 0 & 0 \\ 0 & 1/m & 0 & 0 & 0 & 0 \\ 0 & 0 & 1/m & 0 & 0 & 0 \\ 0 & 0 & 0 & J_{p3} & 0 & J_{r3} \\ 0 & 0 & 0 & 0 & J_{q3} & 0 \\ 0 & 0 & 0 & J_{p4} & 0 & J_{r4} \end{bmatrix} \quad (8)$$

where $J_{p1}, J_{p2} \dots$ denote inertial parameters, and for an inertial matrix of the lander's body:

$$J = \begin{bmatrix} J_{xx} & J_{xy} & J_{xz} \\ J_{xy} & J_{yy} & J_{yz} \\ J_{xz} & J_{yz} & J_{zz} \end{bmatrix}, \quad (9)$$

they are expressed as

$$J_{p1} = -\frac{I_{zz}^2 + I_{xz}^2 - I_{yy}I_{zz}}{I_{xx}I_{zz} - I_{xz}^2}, \quad J_{p2} = -\frac{I_{xz}(I_{yy} - I_{xx} - I_{zz})}{I_{xx}I_{zz} - I_{xz}^2},$$

$$J_{p3} = \frac{I_{zz}}{I_{xx}I_{zz} - I_{xz}^2}, \quad J_{p4} = \frac{I_{xz}}{I_{zz}I_{xx} - I_{xz}^2},$$

$$J_{q1} = -\frac{I_{xz}}{I_{yy}}, \quad J_{q2} = -\frac{I_{xx} - I_{zz}}{I_{yy}}, \quad J_{q3} = \frac{1}{I_{yy}},$$

$$J_{r1} = \frac{I_{xz}(I_{yy} - I_{zz} - I_{xx})}{I_{zz}I_{xx} - I_{xz}^2}, \quad J_{r2} = \frac{I_{xz}^2 + I_{xx}^2 - I_{xx}I_{yy}}{I_{zz}I_{xx} - I_{xz}^2},$$

$$J_{r3} = \frac{I_{xz}}{I_{xx}I_{zz} - I_{xz}^2}, \quad J_{r4} = \frac{I_{xx}}{I_{zz}I_{xx} - I_{xz}^2}.$$

Considering Eq. (3), the coefficient matrix C in Eq. (6) can be expressed such that

$$C = \begin{bmatrix} -\frac{f}{z_c(k)} & 0 & 0 & c_{14}^{(1)} & c_{15}^{(1)} & c_{16}^{(1)} \\ 0 & -\frac{f}{z_c(k)} & 0 & c_{24}^{(1)} & c_{25}^{(1)} & c_{26}^{(1)} \\ \vdots & \vdots & \vdots & \vdots & \vdots & \vdots \\ -\frac{f}{z_c(k)} & 0 & 0 & c_{14}^{(d)} & c_{15}^{(d)} & c_{16}^{(d)} \\ 0 & -\frac{f}{z_c(k)} & 0 & c_{24}^{(d)} & c_{25}^{(d)} & c_{26}^{(d)} \\ 0 & 0 & 1 & 0 & 0 & 0 \end{bmatrix} \quad (10)$$

Therefore, given range images and optical flows for each image frame through conventional image processing technique, the states \mathbf{x} can be calculated by online estimation methods such as an Extended Kalman Filter (EKF)[6]. The algorithm is summarized as follows.

EKF algorithm:

1. Set the initial parameters:

$$\tilde{\mathbf{x}}(0) = \mathbf{x}_0 \in \mathbf{R}^{6 \times 1}, \quad \tilde{P}(0) = \Sigma_0 \in \mathbf{R}^{6 \times 6},$$

$$S = S_0 \in \mathbf{R}^{6 \times 6}, \quad T = T_0 \in \mathbf{R}^{d \times d}.$$

2. Calculate the Kalman Gain ($k = 0, 1, 2, \dots$):

$$K(k) = \tilde{P}(k)C^T(k) \left[C(k)\tilde{P}(k)C^T(k) + T_0 \right]^{-1}.$$

3. Update the state and the covariance estimates ($k = 0, 1, 2, \dots$):

$$\hat{\mathbf{x}}(k) = \tilde{\mathbf{x}}(k) + K(k) [\mathbf{y}(k) - C\tilde{\mathbf{x}}(k)],$$

$$P(k) = \tilde{P}(k) - K(k)C\tilde{P}(k).$$

4. Predict the state and the covariance estimates ($k = 0, 1, 2, \dots$):

$$\tilde{\mathbf{x}}(k+1) = A(\hat{\mathbf{x}}(k)) + B\mathbf{u}(k),$$

$$\tilde{P}(k+1) = \mathbf{a}(k)P(k)\mathbf{a}^T(k) + S_0,$$

where $A(\mathbf{x}(k+1)) = \mathbf{x}(k) + A'(\mathbf{x}(k))\Delta t$ (Δt : enough small sampling time), and $\mathbf{a}(k) =$

$$\left(\frac{\partial A}{\partial \mathbf{x}} \right) \mathbf{x} = \hat{\mathbf{x}}(k).$$

4 Numerical Simulation

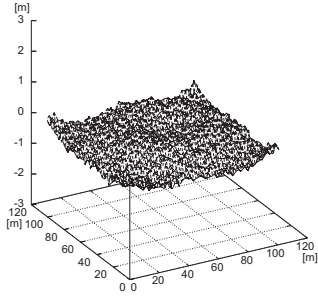


Fig. 2: Digital elevation map of the synthetic terrain for numerical simulation.

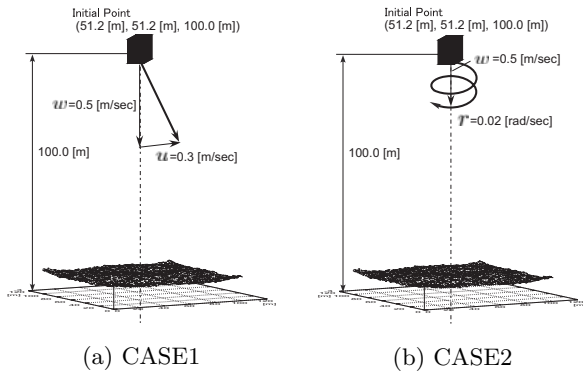


Fig. 3: Simulated lander's motion.

In order to demonstrate the effectiveness of the proposed method, a series of numerical simulations were conducted using a synthetic terrain data. Fig. 2 shows the digital elevation map (DEM) of the synthetic terrain, which is generated by a function combining 2D sinusoidal and 2D fractional Brownian motion[7].

In this simulation study, the lander has a rectangular solid shape ($2.1[\text{m}] \times 2.1[\text{m}] \times 4.8[\text{m}]$) and a weight of $3.0[\text{kg}]$. To see results from different types of the lander's motion two cases are assumed. One considers a constant translational velocity about a horizontal axis and another does a constant angular velocity about a vertical axis as well as a vertical descent motion at a constant velocity for each case as shown in Fig. 3. In both of the cases, the lander's motion is not controlled ($\mathbf{u} = \mathbf{0}$).

Specifications of the 2D scanning LRF are assumed as shown in Table 1, and 32 frames (for 31 seconds) of the range images are applied to the proposed method.

As explained in the previous section, conventional image processing technique (an edge detection with Zero Crossing points and a correlation matching

Table 1: Specifications of the LRF.

Field of view (FOV) [deg \times deg]	10.0 \times 10.0
Frame rate [frame/sec]	1.0
Resolutions [dots]	128 \times 128
Focal length* [m]	1.0
Projection plane's size* [m \times m]	0.35 \times 0.35

*The parameters derived from equivalent CCD camera.

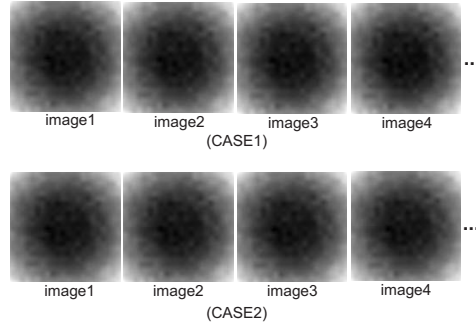


Fig. 4: A range images depicted by grayscale pictures.

method[5]) were applied to extract and track the characteristic scene points ($d = 200$) in the range images from the LRF. Also, considering that the scene points extracted in the first image may go outside of the frames during the tracking operations, the ones to be tracked were chosen near the center of the first image.

When the EKF algorithm was applied to the range image data, the initial parameters were set as

$$\begin{aligned} \Sigma_0 &= 100.0I_6 \text{ (CASE1)}, \text{ or } 10.0I_6 \text{ (CASE2)} \\ S_0 &= \begin{bmatrix} 1.0 \times 10^{-8}I_3 & 0 \\ 0 & 1.0 \times 10^{-8}I_3 \end{bmatrix}, \\ T_0 &= 0.1I_d \text{ (Noise1)}, \text{ or } 0.2I_d \text{ (Noise2)}, \end{aligned}$$

where I_j ($j = 3, 6, d$) denote $j \times j$ identity matrices. The initial values of $\tilde{\mathbf{x}}$ (\mathbf{x}_0) were calculated by applying a least squares method to Eq. (6) for the first range image.

The state and measurement noises in Eqs. (5) and (6) are firstly omitted to generate range images. What we should note here is that measurement errors should occur during the image processing to estimate optical flows, which means that \mathbf{w} in Eq. (6) is not exactly zero during the motion estimation with the EKF algorithm.

Results of the range images are shown in Fig. 4. They are expressed as grayscale pictures, whose darker points depict shorter ranges from the lander's observing point, and vice versa.

Fig. 5 shows estimated optical flows for an image

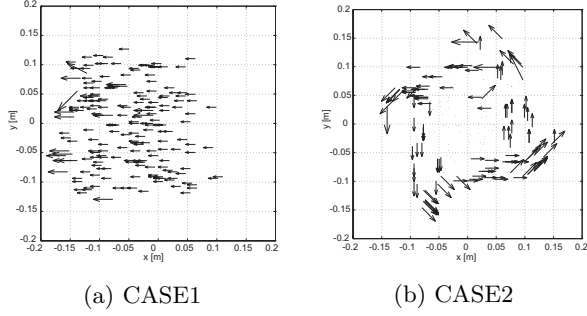


Fig. 5: Estimated optical flows in an image frame. (at $k = 20$ [frames])

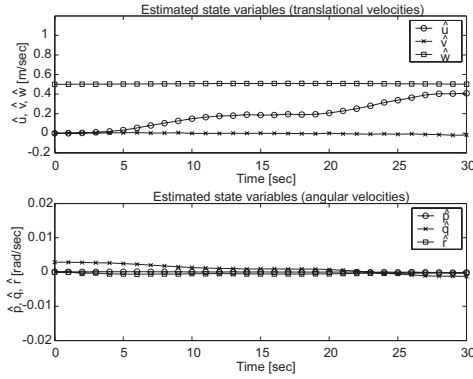


Fig. 6: Estimated parameters of the lander's motion. (CASE1)

frame. As shown in the figures, the optical flows are well estimated so that they distinguish the motion of the scene points depending on the lander's motion.

Figs. 6 and 7 show the lander's translational and rotational velocities estimated with the EKF algorithm. In each figure, time histories of the estimated parameters of translational motion (\hat{u} , \hat{v} , \hat{w}) are shown on the upper side, and those of rotational motion (\hat{p} , \hat{q} , \hat{r}) are shown on the lower side. For both of the cases, most of the parameters except \hat{u} and \hat{q} in CASE1 are successfully estimated. Although in the cases in this paper, unfortunately, the final estimated values of \hat{u} and \hat{q} has slight errors from their exact values, the performance of the online estimation algorithm can be improved by arranging the numbers of the scene points to measure the optical flows and some parameters of the EKF algorithm such as Σ_0 , S_0 and T_0 .

Next, results for the case that the measurement noise is added to the range data are shown in Figs. 8 and 9. A series of Gaussian noise (mean value: 0[m], variance: 0.1[m²]) are added to all the range data in each image frame. As shown in these figures, almost all the estimated parameters are affected by the measurement

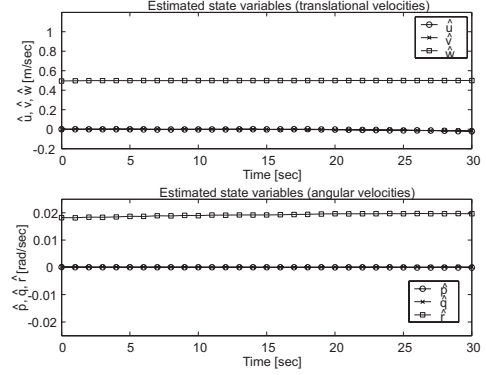


Fig. 7: Estimated parameters of the lander's motion. (CASE2)

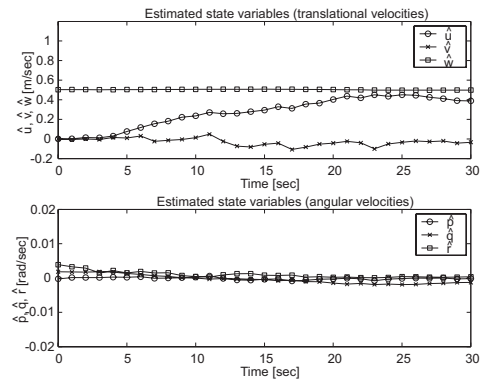


Fig. 8: Estimated parameters of the lander's motion. (CASE1, with measurement noise on the range data)

noise except \hat{w} . Especially in the results for CASE2, it is seen that \hat{r} does not converge on its exact value any more. The reason is considered that as the optical flows in CASE2 (which show the rotating motion around the center of the image frame) are not so simple as those in CASE1, the errors during estimating such flows in each image frame could be more harmful for final motion estimation.

For each case of the lander's motion, the errors of the estimated parameters are evaluated through the error functions defined as,

$$e_t = \frac{1}{3N_f} \times \sum_{k=1}^{N_f} \sqrt{(u(k) - \hat{u}(k))^2 + (v(k) - \hat{v}(k))^2 + (w(k) - \hat{w}(k))^2}, \quad (11)$$

$$e_r = \frac{1}{3N_f} \times \sum_{k=1}^{N_f} \sqrt{(p(k) - \hat{p}(k))^2 + (q(k) - \hat{q}(k))^2 + (r(k) - \hat{r}(k))^2}, \quad (12)$$

where $\hat{\cdot}$ means the estimated values of the parameters, and N_f means the total number of the range images.

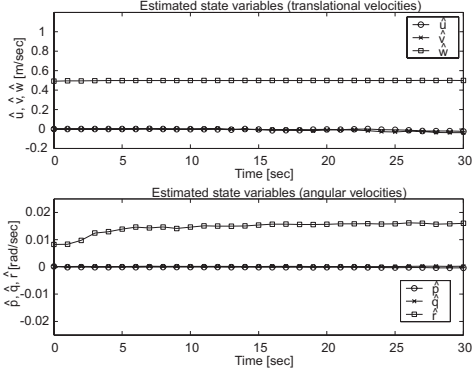


Fig. 9: Estimated parameters of the lander’s motion. (CASE2, with measurement noise on the range data)

The results of the error analysis are shown in Table 2. In the table, ‘Noise1’ means the case that no state and measurement noise are added as shown in Figs. 6 and 7, and ‘Noise2’ means the case that the measurement noise is added to the range data as shown in Figs. 8 and 9. As seen in the table, the measurement noise clearly affects the estimation errors in CASE2 while it is not so serious in CASE1.

Since measurement error included in range image data must have negative effects on estimating optical flows as well as on motion estimation, more sophisticated image processing method should be applied. Also, there remains room for discussing about more effective initial parameters setting (Σ_0 , S_0 , T_0 , etc.) for the EKF algorithm.

Table 2: Error analysis of the lander’s motion estimation.

		Noise1	Noise2
CASE 1	e_t [m/sec]	1.2×10^{-3}	1.0×10^{-3}
	e_r [rad/sec]	1.4×10^{-5}	1.5×10^{-5}
CASE 2	e_t [m/sec]	2.9×10^{-4}	4.8×10^{-4}
	e_r [rad/sec]	0.4×10^{-5}	4.3×10^{-5}

5 Concluding remarks

This study proposes a new approach to estimating lander’s motion from range images of 2D scanning LRF aiming at lander’s autonomous landing. If the range image data can be acquired with enough high resolution and high scanning rate, the proposed method will be effective. On the other hand, the 2D scanning LRF with the specifications assumed in this study have not

been realized yet. Considering the practical specifications of the LRF, the feasibility study on the proposed method to improve motion estimation error should be continued.

References

- [1] T. Kominato et al., “Hayabusa Optical Hybrid Navigation and Guidance”, Proc. of the 16th Workshop on JAXA Astrodynamics and Flight Mechanics, pp. 167-172, 2006.
- [2] H. Morita et al., “Detailed Guidance and Navigation Operations during Descents and Touchdowns, Hayabusa”, Proc. of the 16th Workshop on JAXA Astrodynamics and Flight Mechanics, pp. 173-178, 2006.
- [3] A. Banno, K. Ikeuchi, “Shape Recovery of 3D Data Obtained from a Moving Range Sensor by Using Image Sequences”, Proc. of the 10th IEEE International Conference on Computer Vision (ICCV 2005), pp. 792-799, 2005.
- [4] B. Espiau, F. Chaumette, P. Rives, “A New Approach to Visual Servoing in Robotics”, IEEE Trans. Robotics and Automation, Vol. 8, 3, pp. 313-326, 1992.
- [5] D. A. Forsyth, J. Ponce, “Computer Vision: A Modern Approach”, Prentice Hall, New Jersey, 2003.
- [6] F. L. Lewis, “Optimal Estimation”, John Wiley & Sons, Inc., New York, 1986.
- [7] S. Yoshikawa and K. Nishiguchi, “Generation of Digital Elevation Map of the Moon from Observation Data interpolated by Fractal Modeling”, Transactions of the Society of Instrument and Control Engineers, Vol. 37, No. 3, pp. 262-267, 2001.